Electrochimica Acta 54 (2009) 6861–6875

Contents lists available at ScienceDirect

Electrochimica Acta

journal homepage: www.elsevier.com/locate/electacta

Mesoscopic modeling of two-phase behavior and flooding phenomena in polymer electrolyte fuel cells

Partha P. Mukherjee[a,1], Chao-Yang Wang[a,*], Qinjun Kang[b]

[a] Electrochemical Engine Center (ECEC), and Department of Mechanical and Nuclear Engineering, Pennsylvania State University, University Park, PA 16802, USA
[b] Los Alamos National Laboratory, Los Alamos, NM 87545, USA

ARTICLE INFO

Article history:
Received 16 May 2009
Received in revised form 24 June 2009
Accepted 24 June 2009
Available online 2 July 2009

Keywords:
Polymer electrolyte fuel cell
Two-phase transport
Flooding phenomena
Lattice Boltzmann model
Stochastic microstructure reconstruction

ABSTRACT

A key performance limitation in polymer electrolyte fuel cells (PEFC), manifested in terms of mass transport loss, originates from liquid water transport and resulting flooding phenomena in the constituent components. Liquid water covers the electrochemically active sites in the catalyst layer (CL) rendering reduced catalytic activity and blocks the available pore space in the porous CL and fibrous gas diffusion layer (GDL) resulting in hindered oxygen transport to the active reaction sites. The cathode CL and the GDL play a major role in the mass transport loss and hence in the water management of a PEFC. In this work the development of a mesoscopic modeling formalism coupled with realistic microstructural delineation is presented to study the influence of the pore structure and surface wettability on liquid water transport and interfacial dynamics in the PEFC catalyst layer and gas diffusion layer. The two-phase regime transition phenomenon in the capillary dominated transport in the CL and the influence of the mixed wetting characteristics on the flooding dynamics in the GDL are highlighted.

1. Introduction

Fuel cells, owing to their high energy efficiency, environmental friendliness and low noise, are widely considered as the 21st century energy-conversion devices for mobile, stationary and portable power. Among the several types of fuel cells, the polymer electrolyte fuel cell (PEFC) has emerged as the most promising power source for a wide range of applications.

Despite tremendous recent progress in enhancing the overall cell performance, a pivotal performance limitation in PEFCs is manifested in terms of mass transport loss originating from suboptimal liquid water transport and resulting flooding in the constituent components [1,2]. Liquid water blocks the porous pathways in the CL and GDL thereby causing hindered oxygen transport to the reaction sites as well as covers the electrochemically active sites in the CL leading to increased surface overpotential. This phenomenon is known as "flooding" and is perceived as the primary mechanism leading to the limiting current behavior in the cell performance. The catalyst layer and gas diffusion layer, therefore, play a crucial role in the PEFC water management [1,2] aimed at maintaining a delicate balance between reactant transport from the gas channels and water removal from the electrochemically active sites.

In recent years, there has been an explosion of interest in water management research, evidenced by the development of several macroscopic computational models for two-phase behavior and transport in PEFCs [3–17]. The macroscopic models, reported in the literature, are based on the theory of volume averaging and treat the catalyst layer and gas diffusion layer as macrohomogeneous porous layers. Due to the macroscopic nature, the current models fail to resolve the influence of the structural morphology of the CL and GDL on the underlying two-phase dynamics. Although substantial research, both modeling and experimental, has been conducted to study flooding and water transport in PEFCs, there is serious paucity of fundamental understanding regarding the overall structure–wettability–transport interactions as well as underlying two-phase dynamics in the CL and GDL.

This paper presents the development of a mesoscopic modeling framework to foster enhanced understanding regarding the structure–wettability influence on the underlying two-phase behavior and flooding dynamics in the CL and GDL of a PEFC.

2. Model description

The mesoscopic modeling approach comprises of two components: (1) a stochastic reconstruction method for the generation of the CL and GDL microstructures, and (2) a two-phase lattice Boltzmann method for studying liquid water transport and flooding phenomena in the reconstructed microstructures.

* Corresponding author. Tel.: +1 814 863 4762; fax: +1 814 863 4848.
E-mail addresses: partham@lanl.gov (P.P. Mukherjee), cxw31@psu.edu (C.-Y. Wang).
[1] Present address: Los Alamos National Laboratory, MS T003, Los Alamos, NM 87545, USA. Tel.: +1 505 606 1895; fax: +1 505 665 8737.

0013-4686/$ – see front matter © 2009 Elsevier Ltd. All rights reserved.
doi:10.1016/j.electacta.2009.06.066

2.1. Stochastic microstructure reconstruction model

Detailed description of a porous microstructure is an essential prerequisite for unveiling the influence of pore morphology on the underlying two-phase behavior. This can be achieved either by 3D volume imaging or by constructing a digital microstructure based on stochastic reconstruction models. Non-invasive techniques, such as X-ray micro-tomography, are the popular methods for 3D imaging of pore structure. Additionally, 3D porous structure can be generated using stochastic simulation technique, which creates 3D replicas of the random microstructure based on specified statistical information obtained from high-resolution 2D micrographs of a porous sample. The low cost and high speed of data generation put forth the stochastic generation methods as the preferred choice over the experimental imaging techniques. In this work, CL and GDL microstructures are generated through the development of stochastic reconstruction techniques.

2.2. Catalyst layer microstructure reconstruction

For the electrochemical reaction to occur, the state-of-the-art catalyst layer of a PEFC is a three-phase composite comprising of: (1) ionomer, i.e., the ionic phase which is typically Nafion® to provide a passage for protons to be transported in or out, (2) Pt catalysts supported on carbon, i.e., the electronic phase for electron conduction, and (3) pores for the reactant to be transferred in and product water out. In the present study, the catalyst layer is delineated as a two-phase (pore/solid) structure consisting of the gas phase (i.e., the void space) and a mixed electrolyte/electronic phase (i.e., the solid matrix). The assumption of the mixed electrolyte/electronic phase is well justified from the perspective of ion transport in the electrolyte phase as the limiting mechanism as compared to the electron conduction via the electronic (C/Pt) phase within the CL and henceforth is referred to as the "electrolyte" phase [18–21].

The stochastic reconstruction method is based on the idea that an arbitrarily complex porous structure can be described by a binary phase function which assumes a value 0 in the pore space and 1 in the solid matrix [22]. The intrinsic randomness of the phase function can be adequately qualified by the low order statistical moments, namely porosity and two-point autocorrelation function [22]. Details about the CL microstructure reconstruction along with the underlying assumptions are elaborated in our recent work [18–21], which is based on the stochastic microstructure generation method for unconsolidated porous media reported in Refs. [23,24]. In brief, the stochastic reconstruction technique starts with a Gaussian distribution which is filtered with the two-point autocorrelation function and finally thresholded with the porosity, which creates the 3D realization of the CL structure. The autocorrelation function is computed from a 2D TEM image of an actual CL [18]. The porosity can be calculated by converting the mass loading data of the constituent components available from the CL fabrication process [18]. The pore/solid phase is further distinguished as "transport" and "dead" phase. The basic idea is that a pore phase unit cell surrounded by solid phase-only cells does not take part in species transport and hence in the electrochemical reaction and can, therefore, be treated as a "dead" pore and similarly for the electrolyte phase [18]. The interface between the "transport" pore and the "transport" electrolyte phases is referred to as the electrochemically active area (ECA) and the ratio of ECA and the nominal CL cross-sectional area provides the "ECA-ratio".

Fig. 1 shows the reconstructed microstructure of a typical catalyst coated membrane (CCM) CL with nominal porosity of 60% and thickness of 10 μm along with the input TEM image and the evaluated cross-section averaged pore and electrolyte phase volume fraction distributions across the CL thickness. The cross-section averaged pore/electrolyte volume fraction distribution illustrates the local tortuosity variation along the electrode thickness. Several 3D structures are generated with varying number of unit cells. However, the reconstructed microstructure with the electrochemically active interfacial area ratio complying closely with the experimentally measured value using cyclic voltammerty (CV) is selected for the subsequent simulations. The reconstructed, 3D microstructure with 100 elements in the thickness direction and 50 elements each in the span-wise directions produces an active interfacial area ratio of around 46, which matches reasonably well with the measured CV value (∼45) and thereby reproduces the most important structural parameter responsible for electrochemical activity of the CL. It is important to note that the ECA-ratio varies significantly depending on the electrocatalyst synthesis and electrode fabrication methods, although ideally the ECA-ratio of a beginning-of-life CL should be as high as possible (e.g. >100) for adequate electrochemical performance [25,26]. Since the reconstructed CL microstructure uses a TEM image of an actual CL as an input to evaluate the two-point correlation function which in turn dictates the spatial distribution of the pore/solid phases and hence the electrochemically active interfacial area, therefore a TEM image of a high ECA electrode as an input will lead to a 3D reconstructed CL microstructure with enhanced ECA-ratio.

2.3. Gas diffusion layer microstructure reconstruction

The multi-faceted functionality of a GDL includes reactant distribution, liquid water transport, electron transport, heat conduction and mechanical support to the membrane-electrode-assembly. Carbon-fiber based porous materials, namely non-woven carbon paper and woven carbon cloth, have received wide acceptance as materials of choice for the PEFC GDL owing to their high porosity (∼70% or higher) and good electrical/thermal conductivity. Mathias et al. [27] provided a comprehensive overview of the GDL structure and functions. In this work, the reconstruction of non-woven carbon paper GDL is presented.

The stochastic simulation technique creates 3D realization of the non-woven carbon paper GDL based on structural inputs, namely fiber diameter, fiber orientation and porosity which can be obtained either directly from the fabrication specifications or indirectly from the SEM micrographs or by experimental techniques. Details about the carbon paper GDL microstructure reconstruction along with the underlying assumptions are elaborated in our recent work [28] which is based on the non-woven structure generation technique originally proposed by Schladitz et al. [29]. The specific assumptions made in the reconstruction method, which can however be well justified by inspecting the corresponding carbon paper GDL SEM micrographs, include [28]: (1) the fibers are long compared to the sample size and their crimp is negligible; (2) the interaction between the fibers can be neglected, i.e., the fibers are allowed to overlap; and (3) the fiber system, owing to the fabrication process, is macroscopically homogeneous and isotropic in the material plane, defined as the *xy* plane, which implies that the distribution properties of the stochastic model are invariant with respect to translations as well as rotations about the *z* axis. With these assumptions, the stochastic reconstruction technique can be adequately described as a Poisson line process with one-parametric directional distribution where the fibers are realized as circular cylinders with a given diameter and the directional distribution provides in-plane/through-plane anisotropy in the reconstructed GDL microstructure [28].

Fig. 2 shows the reconstructed microstructure of a typical non-woven, carbon paper GDL with porosity around 72% and thickness of 180 μm along with the structural parameters in terms of the estimated pore size distribution (PSD) and the anisotropy in the in-plane vs. through-plane permeability values.

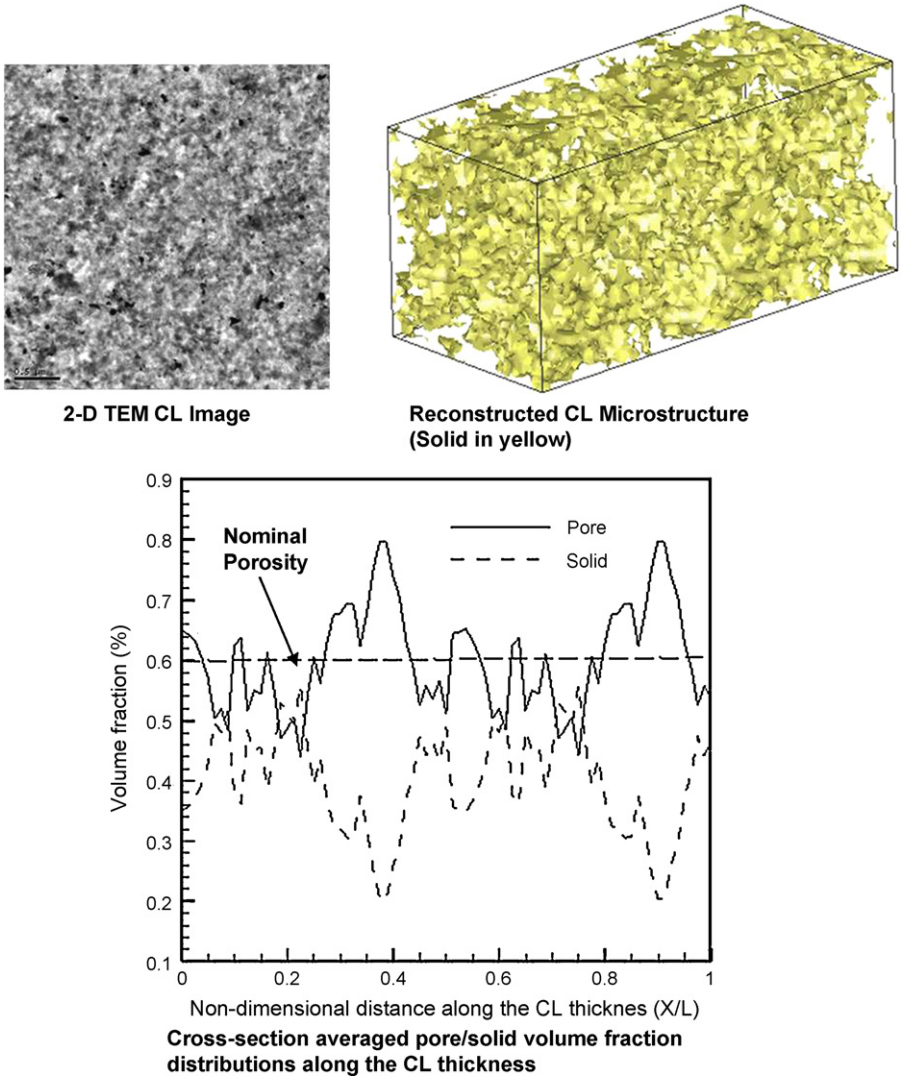

Fig. 1. Reconstructed catalyst layer microstructure along with pore and electrolyte phase volume fractions distribution.

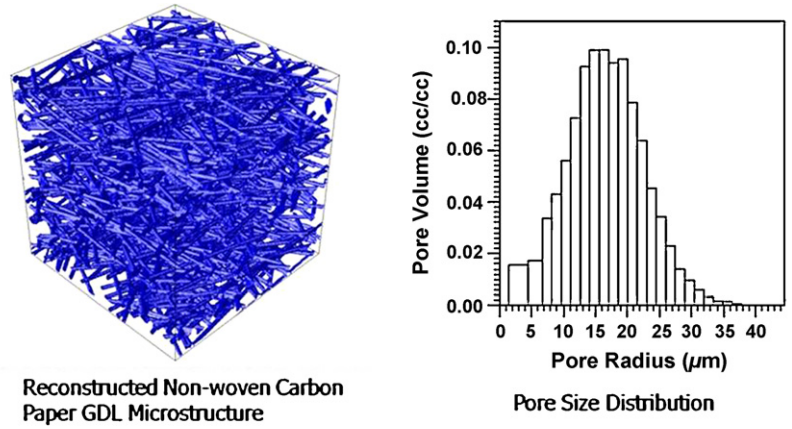

Permeability	In-plane	Through-plane	In-plane/Through-plane
Reconstructed GDL	30.9 darcy	21.1 darcy	1.46
Measured data	33 darcy	18 darcy	1.83

Fig. 2. Reconstructed non-woven carbon paper GDL microstructure along with the evaluated structural properties.

2.4. Lattice Boltzmann model

In recent years, the lattice Boltzmann (LB) method, owing to its excellent numerical stability and constitutive versatility, has developed into a powerful technique for simulating fluid flows and is particularly successful in fluid flow applications involving interfacial dynamics and complex geometries [30]. The LB method is a first-principle based numerical approach. Unlike the conventional Navier–Stokes solvers based on the discretization of the macroscopic continuum equations, lattice Boltzmann methods consider flows to be composed of a collection of pseudo-particles residing on the nodes of an underlying lattice structure which interact according to a velocity distribution function. The lattice Boltzmann method is also an ideal scale-bridging numerical scheme which incorporates simplified kinetic models to capture microscopic or mesoscopic flow physics and yet the macroscopic averaged quantities satisfy the desired macroscopic equations, e.g. Navier–Stokes equation [30]. Due to its underlying kinetic nature, the LB method has been found to be particularly useful in applications involving interfacial dynamics and complex boundaries, e.g. multiphase or multicomponent flows, and flow in porous medium. As opposed to the front-tracking and front-capturing multiphase models in traditional CFD, due to its kinetic nature, the LB model incorporates phase segregation and surface tension in multiphase flow through interparticle force/interactions, which are difficult to implement in traditional methods. While the LB modeling approach better represents the pore morphology in terms of a realistic digital realization of the actual porous medium and incorporates rigorous physical description of the flow processes, it is computationally very demanding. However, because of the inherently parallel nature of the LB algorithm, it is also very efficient running on massively parallel computers [30].

Several LB models have been presented in the literature to study multiphase/multicomponent flows. Gunstensen et al. [31] developed a multicomponent LB model based on a two-component lattice gas model. Shan and Chen [32] proposed a LB model with interparticle potential for multiphase and multicomponent fluid flows. Swift et al. [33] developed a LB multiphase and multicomponent model by using the free-energy approach. He et al. [34] proposed an LB multiphase model using the kinetic equation for multiphase flow. Among the afore-mentioned multiphase LB models, the interaction-potential based approach is widely used due to its simplicity in implementing boundary conditions in complex porous structures and remarkable versatility in terms of handling fluid phases with different densities, viscosities and wettabilities, as well as the capability of incorporating different equations of state. In this work, we have developed the interaction-potential based two-phase LB model to study the structure–wettability influence on the underlying two-phase dynamics in the CL and GDL of a PEFC.

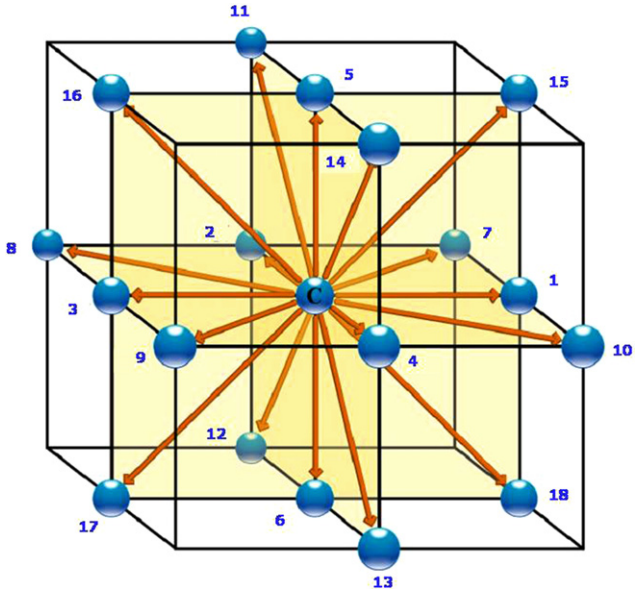

Fig. 3. Schematic of D3Q19 lattice structure.

2.5. Two-phase LB model description

The interaction-potential model, originally proposed by Shan and Chen [32], and henceforth referred to as the S–C model, introduces k distribution functions for a fluid mixture comprising of k components. Each distribution function represents a fluid component and satisfies the evolution equation. The non-local interaction between particles at neighboring lattice sites is included in the kinetics through a set of potentials. The LB equation for the kth component can be written as:

$$f_i^k(\mathbf{x}+\mathbf{e}_i\delta_t, t+\delta_t) - f_i^k(\mathbf{x}, t) = -\frac{f_i^k(\mathbf{x}, t) - f_i^{k(\mathrm{eq})}(\mathbf{x}, t)}{\tau_k}, \tag{1}$$

where $f_i^k(\mathbf{x}, t)$ is the number density distribution function for the kth component in the ith velocity direction at position $\mathbf{x}$ and time t, and δ_t is the time increment. In the term on the right-hand side, τ_k is the relaxation time of the kth component in lattice unit, and $f_i^{k(\mathrm{eq})}(\mathbf{x}, t)$ is the corresponding equilibrium distribution function. The right-hand-side of Eq. (1) represents the collision term, which is simplified to the equilibrium distribution function $f_i^{k(\mathrm{eq})}(\mathbf{x}, t)$ by the so-called BGK (Bhatnagar–Gross–Krook), or the single-time relaxation approximation [35]. The spatio-temporal discrete form of the LB evolution equation based on the BGK approximation, given by Eq. (1), is often referred to as the LBGK equation. For a three-dimensional 19-speed lattice (D3Q19, where D is the dimension and Q is the number of velocity directions), the schematic of which is shown in Fig. 3 with the velocity directions, the equilibrium distribution function, $f_i^{k(\mathrm{eq})}(\mathbf{x}, t)$, assumes the following form [36,37]:

$$\left.\begin{aligned} f_0^{k(\mathrm{eq})} &= \beta_k n_k - \frac{1}{2} n_k \mathbf{u}_k^{\mathrm{eq}} \cdot \mathbf{u}_k^{\mathrm{eq}}, \\ f_i^{k(\mathrm{eq})} &= \frac{1-\beta_k}{12} n_k + \frac{1}{6} n_k (\mathbf{e}_i \cdot \mathbf{u}_k^{\mathrm{eq}}) + \frac{1}{4} n_k (\mathbf{e}_i \cdot \mathbf{u}_k^{\mathrm{eq}})^2 - \frac{1}{12} n_k \mathbf{u}_k^{\mathrm{eq}} \cdot \mathbf{u}_k^{\mathrm{eq}}, \quad \text{for } i = 1, \ldots, 6, \\ f_i^{k(\mathrm{eq})} &= \frac{1-\beta_k}{24} n_k + \frac{1}{12} n_k (\mathbf{e}_i \cdot \mathbf{u}_k^{\mathrm{eq}}) + \frac{1}{8} n_k (\mathbf{e}_i \cdot \mathbf{u}_k^{\mathrm{eq}})^2 - \frac{1}{24} n_k \mathbf{u}_k^{\mathrm{eq}} \cdot \mathbf{u}_k^{\mathrm{eq}}, \quad \text{for } i = 7, \ldots, 18. \end{aligned}\right\} \tag{2}$$

In the above equations, the discrete velocities, $\mathbf{e}_i$, are given by:

$$\mathbf{e}_i = \begin{cases} (0,0,0), & i = 0, \\ (\pm 1,0,0), (0,\pm 1,0), (0,0,\pm 1), & i = 1\text{–}6, \\ (\pm 1,\pm 1,0), (\pm 1,0,\pm 1), (0,\pm 1,\pm 1), & i = 7\text{–}18. \end{cases} \tag{3}$$

The free parameter, β_k, relates to the speed of sound of a region of pure kth component, as:

$$(c_s^k)^2 = \frac{1-\beta_k}{2}. \tag{4}$$

The number density of the kth component, n_k, is defined as:

$$n_k = \sum_i f_i^k, \tag{5}$$

The mass density of the kth component is defined as:

$$\rho_k = m_k n_k = m_k \sum_i f_i^k. \tag{6}$$

The fluid velocity of the kth fluid is defined through:

$$\rho_k \mathbf{u}_k = m_k \sum_i \mathbf{e}_i f_i^k, \tag{7}$$

where m_k is the molecular mass of the kth component.

The equilibrium velocity, $\mathbf{u}_k^{\mathrm{eq}}$, is determined by the expression:

$$\rho_k \mathbf{u}_k^{\mathrm{eq}} = \rho_k \mathbf{u}' + \tau_k \mathbf{F}_k, \tag{8}$$

where $\mathbf{u}'$ is a common or base velocity on top of which an extra component-specific velocity due to interparticle interaction is added for each component. Interparticle interaction is realized through the total force, $\mathbf{F}_k$, acting on the kth component, including fluid/fluid interaction $\mathbf{F}_{1k}$, fluid/solid interaction, $\mathbf{F}_{2k}$, and external force $\mathbf{F}_{3k}$ [37] and is expressed as:

$$\mathbf{F}_k = \mathbf{F}_{1k} + \mathbf{F}_{2k} + \mathbf{F}_{3k}. \tag{9}$$

The conservation of momentum at each collision in the absence of interaction force (i.e., in the case of $\mathbf{F}_k = 0$), requires $\mathbf{u}'$ to satisfy the following relation:

$$\mathbf{u}' = \frac{\sum_{k=1}^{s} \rho_k \mathbf{u}_k / \tau_k}{\sum_{k=1}^{s} \rho_k / \tau_k}. \tag{10}$$

A simple long-range interaction force between particles of the kth component at site $\mathbf{x}$ and the $\bar{k}$th component at site $\mathbf{x}'$ is introduced and the total fluid/fluid interaction force on the kth component at site $\mathbf{x}$ is given by:

$$\mathbf{F}_{1k}(\mathbf{x}) = -\psi_k(\mathbf{x}) \sum_{\mathbf{x}'} \sum_{\bar{k}=1}^{s} G_{k\bar{k}}(\mathbf{x}, \mathbf{x}') \psi_{\bar{k}}(\mathbf{x}')(\mathbf{x}' - \mathbf{x}), \tag{11}$$

where $G_{k\bar{k}}(\mathbf{x}, \mathbf{x}')$ is Green's function and satisfies $G_{k\bar{k}}(\mathbf{x}, \mathbf{x}') = G_{k\bar{k}}(\mathbf{x}', \mathbf{x})$. It reflects the intensity of interparticle interaction. $\psi_{k\bar{k}}(\mathbf{x})$ is called the "effective number density" and is defined as a function of $\mathbf{x}$ through its dependency on the local number density, $\psi_k = \psi_k(n_k)$. In the D3Q19 lattice model, the interaction potential couples nearest and next-nearest neighbors and the Green's function is given by:

$$G_{k\bar{k}}(\mathbf{x}, \mathbf{x}') = \begin{cases} g_{k\bar{k}}, & |\mathbf{x} - \mathbf{x}'| = 1, \\ g_{k\bar{k}}/2, & |\mathbf{x} - \mathbf{x}'| = \sqrt{2}, \\ 0, & \text{otherwise}, \end{cases} \tag{12}$$

where $g_{k\bar{k}}$ represents the strength of interparticle interactions between component k and $\bar{k}$. The effective number density, $\psi_k(n_k)$ is taken as n_k in the present model and other choices will give a different equation of state (EOS). The interactive force between the fluid and wall is realized by considering the wall as a separate phase with constant number density and is given by [38]:

$$\mathbf{F}_{2k}(x) = -n_k(\mathbf{x}) \sum_{\mathbf{x}'} g_{k\mathrm{w}} n_{\mathrm{w}}(\mathbf{x}')(\mathbf{x}' - \mathbf{x}), \tag{13}$$

where n_{w} is the number density of the wall, which is a constant at the wall and zero elsewhere, $g_{k\mathrm{w}}$ is the interaction strength between kth component and the wall. The interactive strength, $g_{k\mathrm{w}}$, defines the wall wettability, and is positive for a non-wetting fluid and negative for a wetting fluid. It is to be noted that $\mathbf{F}_{2k}$ is perpendicular to the wall and will not affect the no-slip boundary condition. The action of a constant body force can be incorporated as:

$$F_{3k} = \rho_k \mathbf{g} = m_k n_k \mathbf{g}, \tag{14}$$

where $\mathbf{g}$ is the constant body force per unit mass.

The continuity and momentum equations can be obtained for the fluid mixture as a single fluid using Chapman–Enskog expansion procedure in the nearly incompressible limit [38]:

$$\left.\begin{aligned} &\frac{\partial \rho}{\partial t} + \nabla \cdot (\rho \mathbf{u}) = 0, \\ &\rho \left[\frac{\partial u}{\partial t} + (\mathbf{u} \cdot \nabla)\mathbf{u} \right] = -\nabla p + \nabla \cdot [\rho \nu (\nabla \mathbf{u} + \mathbf{u} \nabla)] + \rho \mathbf{g}, \end{aligned}\right\} \tag{15}$$

where the total density and velocity of the fluid mixture are given, respectively, by [39]:

$$\left.\begin{aligned} &\rho = \textstyle\sum_k \rho_k, \\ &\rho \mathbf{u} = \textstyle\sum_k \rho_k \mathbf{u}_k + \frac{1}{2} \sum_k \mathbf{F}_k. \end{aligned}\right\} \tag{16}$$

The pressure, which is usually a non-ideal gas equation of state, is given by [38]:

$$p = \sum_k \frac{(1 - \beta_k) m_k n_k}{2} + 3 \sum_{k,\bar{k}} g_{k\bar{k}} \psi_k \psi_{\bar{k}}. \tag{17}$$

In the present model, $m_k = 1$ and $\beta_k = 1/3$, which is commonly used in the literature. Then the equation of state can be written as:

$$p = \sum_k \frac{n_k}{3} + 3 \sum_{k,\bar{k}} g_{k\bar{k}} \psi_k \psi_{\bar{k}}. \tag{18}$$

The viscosity is given by:

$$\nu = \frac{\sum_k \alpha_k \tau_k - 1/2}{3}, \tag{19}$$

where α_k is the mass density concentration of the kth component and is defined as [40]:

$$\alpha_k = \frac{\rho_k}{\sum_k \rho_k}. \tag{20}$$

It should be noted that the introduction of fluid/solid interaction has no effect on the macroscopic equations since $\mathbf{F}_{2k}$ exists only at the fluid/solid interface. This model has been shown to satisfy Galilean invariance [39]. Furthermore, in this interparticle potential model, the separation of a two-phase fluid into its components is automatic [32].

2.6. Two-phase LB model calibration

The primary physical parameters, such as the fluid/fluid and fluid/solid interaction parameters, need a priori evaluation through model calibration using numerical experiments. The fluid/fluid interaction gives rise to the surface tension force and the fluid/solid interaction manifests in the wall adhesion force. In this regard, two numerical experiments are conducted: (1) ***bubble test*** in the absence of solid phase to evaluate the fluid/fluid interaction parameter, and (2) ***static droplet test*** in the presence of solid wall to determine the fluid/solid interaction parameter.

2.7. Bubble test

In order to evaluate the fluid/fluid interaction parameter, which takes care of the fluid/fluid surface tension and hence one of the most important physical input parameters for the D3Q19 two-phase S–C model, bubble test is performed in the absence of solid phase according to the procedure outlined by Hou et al. [40].

The three-dimension bubble test consisted of a spherical non-wetting phase (NWP) initially located at the center of a $50 \times 50 \times 50$

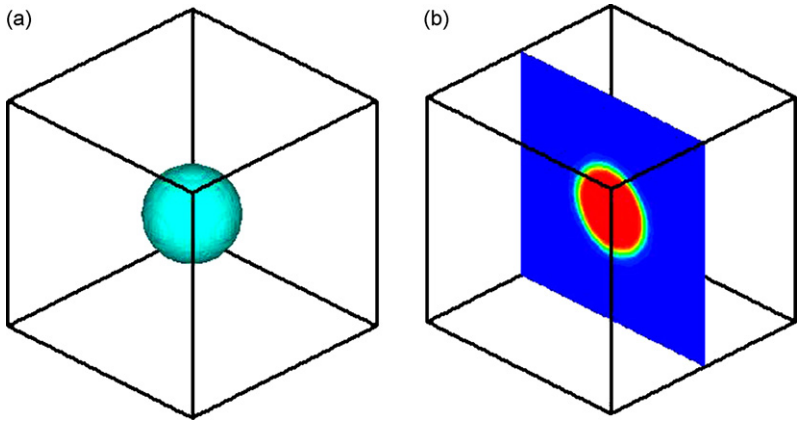

Fig. 4. (a) Steady state bubble; (b) NWP density contour at the mid-plane, exhibiting phase separation.

(in lattice units) domain. Initially, a NWP bubble with a certain radius was completely immersed in the wetting-phase (WP), otherwise occupying the entire domain. Periodic boundary conditions were applied in all three coordinate directions. At equilibrium (steady) state, in the absence of any solid phase and body force, each fluid has a constant density and pressure across the interface. The pressure jump across the interface is determined by the radius of the bubble and the surface tension is given by Laplace's law as:

$$\Delta P = P_c = P_2 - P_1 = \frac{2\sigma}{R_0}. \quad (21)$$

It should be noted that 1 refers to the wetting phase and 2 refers to the non-wetting phase respectively and this convention will be used in the rest of this paper. Since the LB method is a dynamic technique, the static bubble is achieved through time evolution and the size of the final bubble and final densities are unknown at the initial time.

The model input parameters for the bubble test are: initial densities, ρ_1 and ρ_2, of the WP and NWP outside and inside the bubble respectively, the relaxation times, τ_1 and τ_2, and fluid/fluid interaction coefficient, $g = g_{12} = g_{21}$. It should be noted that all the units are in lattice units unless otherwise stated specifically.

The initial fluid densities were specified as $\rho_2 = 150$ and $\rho_1 = 0$ inside the bubble, and $\rho_2 = 0$ and $\rho_1 = 150$ outside the bubble, based on the work by Pan et al. [41,42]. The relaxation times, $\tau_1 = 1$ and $\tau_1 = 1.42$ are considered. Steady state was considered achieved when the relative difference of the overall fluid velocity, given by Eq. (16), at a time step T and at $(T - 1000)$ was of the order of 10^{-6}.

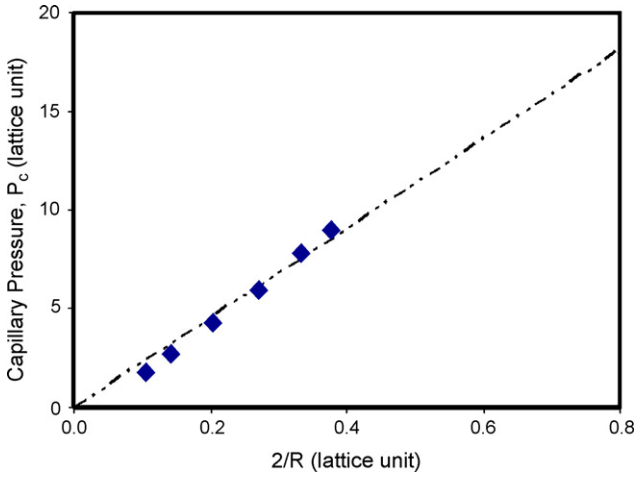

Fig. 5. Bubble test confirming Laplace's law.

If steady state cannot be reached, the simulation time was set to a maximum of 40,000 time steps in lattice units. The fluid/fluid interaction coefficient, g, was set to 0.001 and it was sufficient to produce the desired fluid separation.

Fig. 4 shows the density contour of the non-wetting phase at the mid-section along with the static bubble formed at steady state with the initial bubble radius, $R_{init} = 10$. The steady state bubble radius, R, was evaluated using the procedure described by Hou et al. [40]. Fig. 4 clearly suggests that the two fluids have separated with the chosen fluid/fluid interaction parameter. It also depicts that the S–C LB model essentially follows the diffuse interface approach evidenced by the finite interface formed between the two phases. The fluid pressures across the interface were measured using Eq. (18) after steady state was achieved. To test Laplace's law, given by Eq. (21), the bubble test was conducted for several initial bubble radii. The variation of pressure difference across the interface with respect to $(2/R)$ is plotted in Fig. 5 and it exhibits good agreement with Laplace's law. The slope of the linear fit is the interfacial tension, σ, which was calculated as 22.62 in lattice units for the present bubble test simulation.

2.8. Static droplet test

In order to evaluate the fluid/solid interaction parameter for the D3Q19 two-phase S–C LB model, which controls the wall wettability effect through the resulting contact angle at the solid/fluid/fluid interface, a static droplet test is performed in the presence of a solid wall.

The static contact angle is represented by the fluid/solid interaction parameter, g_{kw}, as illustrated in Eq. (13). In the present contact angle simulation, initially a half liquid droplet of radius 10, in lattice units, is placed at the geometric center of the bottom solid wall of the $50 \times 50 \times 50$ (in lattice units) computational domain with periodic boundary conditions (BCs) in the x direction and wall BCs in the y and z directions. In this simulation no body force is applied and similar convergence criterion, as in the case of bubble test, is maintained. The input parameters remain the same as in the case of the

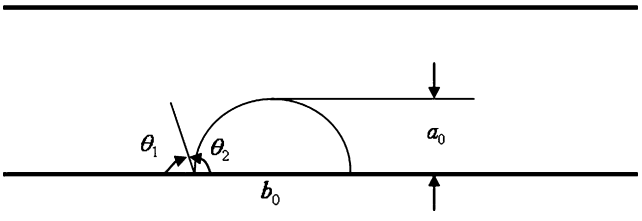

Fig. 6. Schematic illustration of droplet contact angle determination parameters.

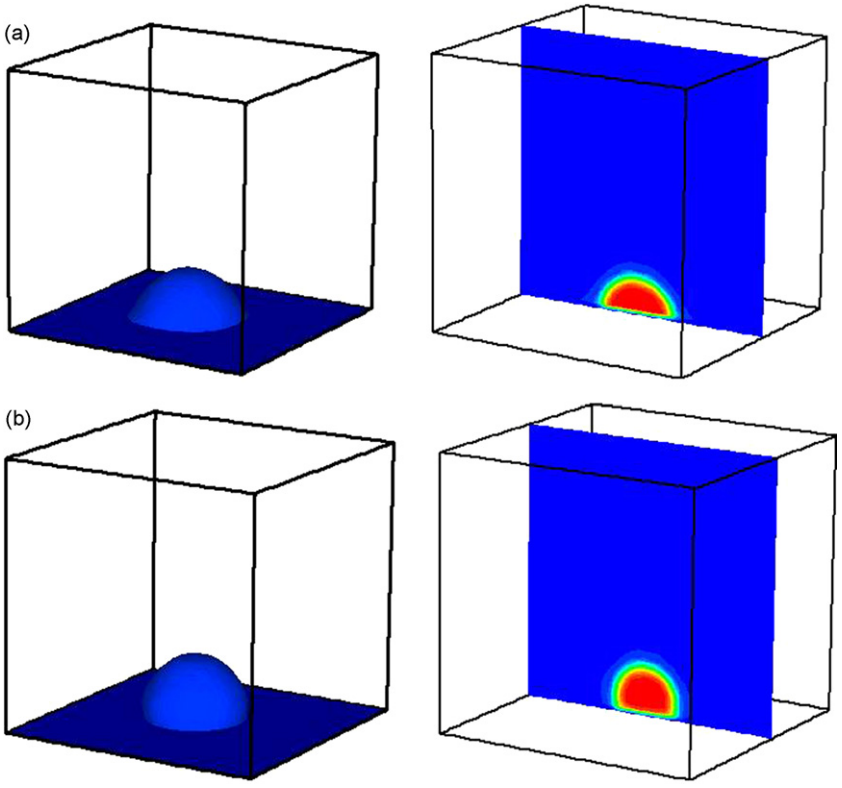

Fig. 7. Varying wettability with different fluid/solid interaction parameters: (a) $g_{2w} = -0.02$, $\theta = 78.05^\circ$; (b) $g_{2w} = 0.05$, $\theta = 117.7^\circ$.

bubble test with the additional fluid/solid interaction parameter, $g_{1w} = -g_{2w}$. A particle distribution function bounce-back scheme [43] is used at the walls to obtain no-slip boundary condition. The bounce-back scheme implies that when a particle distribution streams to a wall node, it scatters back to the node it originated from.

When a static droplet is formed, the contact angle is evaluated from the final steady state values of the droplet radius, R, droplet height, a_0, and wet length of the droplet, b_0, using the following relation [44] and as illustrated in the schematic in Fig. 6:

$$\tan(\theta_2) = \frac{b_0}{2(R - a_0)}. \tag{22}$$

The final radius, R, is evaluated from a_0 and b_0, using the following expression [44]:

$$R = \frac{a_0}{2} + \frac{b_0^2}{8a_0}. \tag{23}$$

Hereafter, for simplicity,θ_2 is referred to as the contact angle,θ.

The values of g_{1w} and g_{2w} are varied to obtain steady droplets with different contact angles. Fig. 7 shows two contact angles obtained by adjusting the fluid/solid interaction parameter as well as the density contours of the droplet fluid at the mid-section. Fig. 8 depicts that the contact angle is a function of g_{2w}, which is in agreement with the predictions reported in earlier works by Yang et al. [45] and Kang et al. [46]. As shown in Fig. 8, a negative value of g_{2w} gives rise to a contact angle less than 90°, indicating that phase 2 tends to wet the surface leading to hydrophilic wettability. A contact angle greater than 90° is formed when g_{2w} is positive; indicating that phase 2 is non-wetting and the wettability condition is termed as hydrophobic [46,47]. For $g_{2w} = 0$, neither of the phases exhibits preferential wetting to the surface, which is defined as neutral wetting situation.

3. Two-phase simulation

Before discussing the details of the numerical experiments performed in this study, the primary mechanisms governing the two-phase transport in the PEFC catalyst layer and gas diffusion layer are discussed, which essentially build the foundations behind the specific assumptions and justifications pertaining to the subsequent two-phase simulations.

3.1. Two-phase transport mechanism

For two-phase flow through the porous catalyst layer and the fibrous gas diffusion layer in a PEFC, due to the complex structure

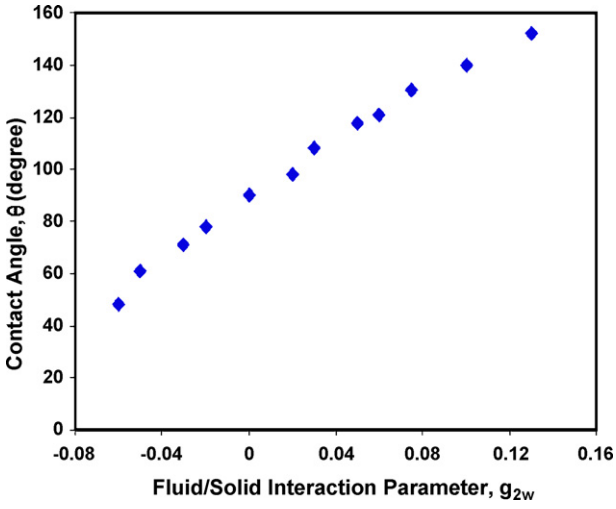

Fig. 8. Contact angle, θ, as a function of fluid/solid interaction parameter, g_{2w}.

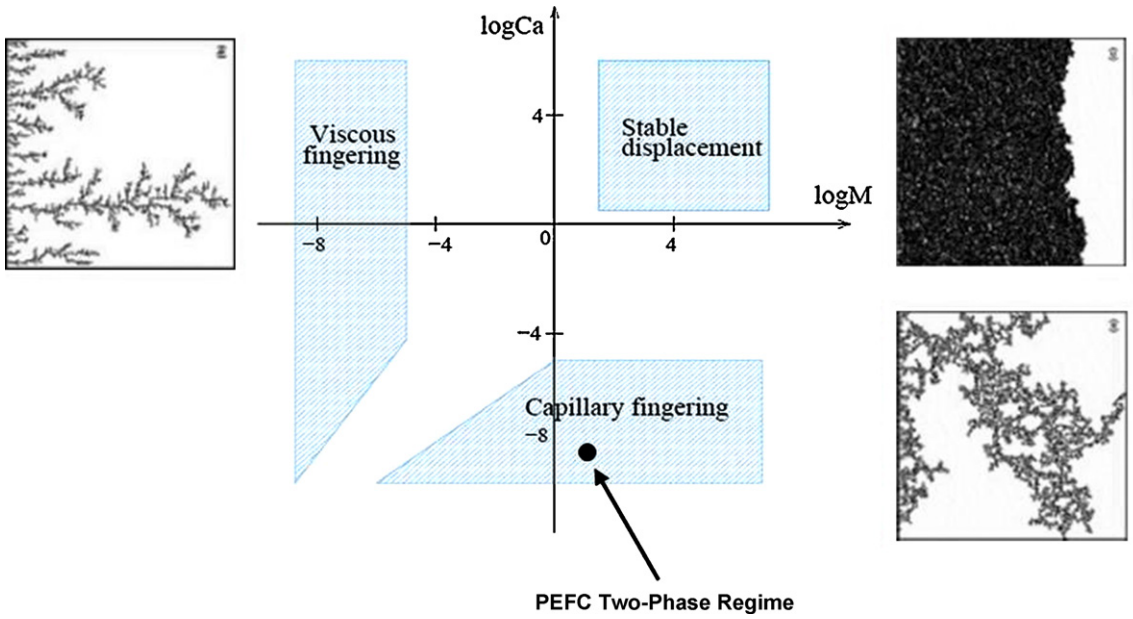

Fig. 9. Phase diagram along with fluid displacement patterns [48,49].

as well as significantly small pore size, e.g. around 0.05–0.1 μm in the CL and 20–30 μm in the GDL, surface forces become dominant as compared to the gravity, viscous and inertia forces. In this regard, the representative values of the salient non-dimensional numbers governing the underlying transport in the CL are listed below. For a representative CL, the order of magnitude of the following non-dimensional numbers can be estimated as:

$$\text{Reynolds number}: \quad \text{Re} = \frac{\rho_2 U_2 D}{\mu_2} \sim 10^{-4},$$

$$\text{Capillary number}: \quad \text{Ca} = \frac{\mu_2 U_2}{\sigma} \sim 10^{-6},$$

$$\text{Bond number}: \quad \text{Bo} = \frac{g(\rho_2 - \rho_2)D^2}{\sigma} \sim 10^{-10},$$

$$\text{Weber number}: \quad \text{We} = \frac{\rho_2 U_2^2 D}{\sigma} = \text{Re} \cdot \text{Ca} \sim 10^{-10},$$

U_2 and μ_2 are the non-wetting phase velocity and dynamic viscosity respectively; σ is the surface tension and g is the gravitational acceleration. U_2 Similarly, the afore-mentioned non-dimensional parameters exhibit very low values in the GDL within comparable order of magnitude variations. It should be noted that for the hydrophobic CL and GDL representative of a typical polymer electrolyte fuel cell system, water is the non-wetting phase (NWP) and air the wetting phase (WP). As mentioned earlier, in this paper, we identify the non-wetting phase with subscript 2 and the wetting phase with 1. From the Bond number, defined as the ratio of gravitational force to the surface tension force, it is evident that the effect of gravity is negligible with respect to the surface tension force, thus indicating strong capillary force dominance. Also within PEFC electrodes, velocity, U_2 is significantly small. Now, from the Reynolds number, representing the ratio of inertia force to viscous force, it is obvious that the inertial effect is negligible, as compared to the viscous force. Combining the implications of low Reynolds and Bond numbers, it can be inferred that the density ratio, which is ~1000 for air-water two-phase flow for the PEFC operation, should have significantly small influence on the overall transport in the CL and GDL. Now, from the Capillary number, Ca, which represents the ratio of viscous force to the surface tension force, it can be observed that the effect of viscous force is also negligible as compared to the surface tension force. Apart from these non-dimensional numbers, the Weber number (We), defining the ratio of inertial force to the surface tension force, which is also a product of Re and Ca, emphasizes the fact that the effects of inertia and viscous forces are truly insignificant as compared to the surface tension force representative of two-phase transport in the PEFC CL and GDL. It should be noted that the viscosity ratio for the non-wetting and wetting phases in a fuel cell operating at 80 °C is estimated to be, ~18. Based on the calculated $M = \mu_2/\mu_1$ representative viscosity ratio and capillary number values, the typical operating two-phase regime for the CL and GDL belongs to the capillary fingering zone on the "phase diagram" proposed by Lenormand et al. [48], and is shown in Fig. 9. The notion of the "phase diagram", proposed by Lenormand et al. [48], is based on their experiment, involving immiscible displacement of a wetting phase by a non-wetting phase, in a flat and horizontal porous medium where gravity forces were neglected. This phase diagram further bolsters the validity of our assumption that for air–water two-phase flow in the CL and GDL of a PEFC, the viscous forces are truly negligible and the principal force is owing to the action of capillarity, which would consequently lead to capillary fingering type displacement pattern. Viscous fingering pattern is observed at low viscosity ratio (M), where the principal force is the viscous force of the resident fluid and the capillary force and pressure drop in the displacing fluid can be neglected. In the stable displacement flow regime, representative of high M and high Ca, the principal force is due to the viscosity of the displacing fluid and capillary effects in the resident fluid are negligible. Typical fluid displacement patterns pertaining to the three flow regimes are also shown in Fig. 9 along with the phase diagram and are adapted from the work by Ewing and Berkowitz [49], who extended the two-dimensional phase diagram by Lenormand et al. [48] to a three-dimensional phase diagram by adding the effect of gravity force through Bond number (Bo) in the third direction. However, in general, the effect of gravity force in the overall fuel cell system, let alone in the porous catalyst layer and gas diffusion layer, has been shown to be truly insignificant [50]. Using this analysis, it can be safely adjudged that for modeling air–water two-phase transport in the PEFC CL and GDL the effects of high density ratio (~1000) and viscosity ratio (~18) variation can be assumed to be negligible represented by the significantly low capillary number. Apropos of

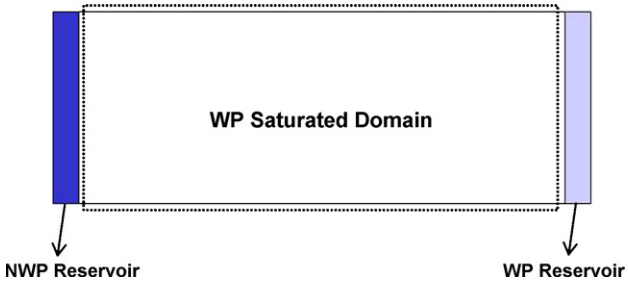

Fig. 10. Schematic diagram of the immiscible two-phase displacement simulation setup.

this justification, in the present two-phase LB model, comparable density and viscosity values of the non-wetting and wetting phases are assumed.

3.2. Two-phase numerical experiments and setup

In this study, two numerical experiments are specifically designed for investigating liquid water transport and two-phase dynamics through the reconstructed CL and GDL microstructures. It should be noted that the primary objective of the numerical experiments is to study, in an ***ex situ setup***, the influence of the microstructure and wetting characteristics on the underlying two-phase behavior and flooding dynamics in the PEFC porous catalyst layer and fibrous gas diffusion layer. Additionally, in the subsequent two-phase numerical simulations, isothermal condition is assumed as a first and reasonable approximation, i.e., the thermal effects on the two-phase behavior are not considered. It is worth mentioning that although the thermal effect in the thin CL could be well neglected, the heat pipe effect in the GDL two-phase transport [6] could be important. However, the development of non-isothermal, two-phase LB model with phase change effects is left as a future exercise.

The first numerical setup is devised to simulate a ***quasi-static displacement experiment***, detailed elsewhere in the literature in the context of geologic porous media transport [51,52], for simulating immiscible, two-phase transport through the CL and GDL structures. Fig. 10 schematically shows the computational domain and setup of the displacement simulation, i.e., ***primary drainage*** experiment. A NWP reservoir is added to the porous structure at the front end and a WP reservoir is added at the back end [20,41]. These two end reservoirs added to the CL/GDL domain in the through-plane (i.e., thickness) direction are composed of void space. It should be noted that for the primary drainage (PD) simulation in the hydrophobic CL and GDL, liquid water is the NWP and air is the WP.

Fixed pressure boundary conditions, which are equivalent to fixed densities within the LB framework, are imposed at the first layer of the NWP reservoir and the last layer of the WP reservoir. Fixed pressure boundary conditions are implemented by assigning the equilibrium distribution functions, computed with zero velocity and specified density at the reservoirs, to the distribution functions [53]. Periodic boundary conditions are applied in the span-wise directions. A particle distribution function bounce-back scheme [43] is used at the walls to obtain no-slip boundary condition.

The primary drainage process is simulated starting with zero capillary pressure, by fixing the NWP and WP reservoir pressures to be equal. Then the capillary pressure is increased incrementally by decreasing the WP reservoir pressure while maintaining the NWP reservoir pressure at the fixed initial value. The pressure gradient drives liquid water into the initially air-saturated CL and GDL by displacing it. A lattice site is assumed occupied by the NWP if the NWP density at that node is larger than half of the fixed NWP density; otherwise the node is assumed to be occupied by the WP. For each capillary pressure, the steady state is assumed achieved when, either the relative difference of the overall fluid velocity given by Eq. (16) over 1000 time steps is of the order of 10^{-6} or the NWP saturation shows negligible variation after 1000 time steps, whichever occurs first. It is worth mentioning that the current primary drainage simulation corresponds to an ex situ experimental procedure where the CL or the GDL structure is not a part of an operational fuel cell. The primary objective of the quasi-static displacement simulation is to study liquid water behavior through the porous CL and fibrous GDL structures and the concurrent response to capillarity as a direct manifestation of the underlying pore-morphology.

In order to achieve enhanced fundamental insight into the underlying two-phase transport and interfacial dynamics, another numerical experiment is designed based on the ***steady-state flow experiment***, typically devised in the petroleum/reservoir engineering applications and detailed elsewhere in the literature [51,52]. Briefly, in the steady-state flow experiment the two immiscible fluids are allowed to flow simultaneously until equilibrium is attained and the corresponding saturations, fluid flow rates and pressure gradients can be directly measured and correlated using Darcy's law. The term "steady-state", however needs to be duly qualified in the sense that the process is intrinsically a dynamical equilibrium of two moving fluids, although macroscopically stable [54]. In the *steady-state flow simulation*, initially both the NWP and WP are randomly distributed throughout the CL and GDL porous structures such that the desired NWP saturation is achieved [20]. The initial random distribution of the liquid water phase (i.e., NWP) in the otherwise air (i.e., WP) occupied CL closely represents the physically perceived scenario of liquid water generation due to the electrochemical reaction at different catalytically active sites within the CL structure and subsequent transport by the action of capillarity. Furthermore, in the case of recent ultra-thin CL structures and also conventional catalyst layers characterized by very low hydrophobicity, liquid water generated in the CL fails to overcome the capillary pressure barrier imposed by the sufficiently hydrophobic microporous layer (MPL) situated between the CL and GDL. In this scenario, only water vapor transports into the GDL and condenses into liquid water at several preferential sites throughout the GDL which subsequently transports due to the action of capillarity [20,55]. These two scenarios form the basis for the present dynamical equilibrium immiscible flow simulation. In this numerical experiment, the computational domain is assumed to be bounded by walls in the span-wise directions and periodic in the through-plane/thickness direction consistent with the numerical setup described in the context of geologic porous media transport reported by Li et al. [56]. Counter-current flow is simulated by applying a body force for both the phases along the flow direction which mimics the redistribution of the phases under the capillary force corresponding to the typical capillary number (Ca $\sim 10^{-6}$). Steady state is considered attained when the saturation and flow rates of both phases exhibit infinitesimal change over 1000 time steps.

For efficient simulation of two-phase transport through the porous structures with sufficiently large number of lattice points along with the computational intensive nature of the particle-based LB modeling approach, the present two-phase LB model is parallelized based on full lattice representation (FLR) where both the fluid and solid nodes are stored and computed on a regular computational grid [20]. With the FLR approach, the parallelization is implemented based on 1D slice decomposition along the thickness/through-plane direction using the standard Message Passing Interface (MPI) library. In order to keep the computational cost within a reasonable limit and without losing much on accuracy the simulations presented in this study are performed on a

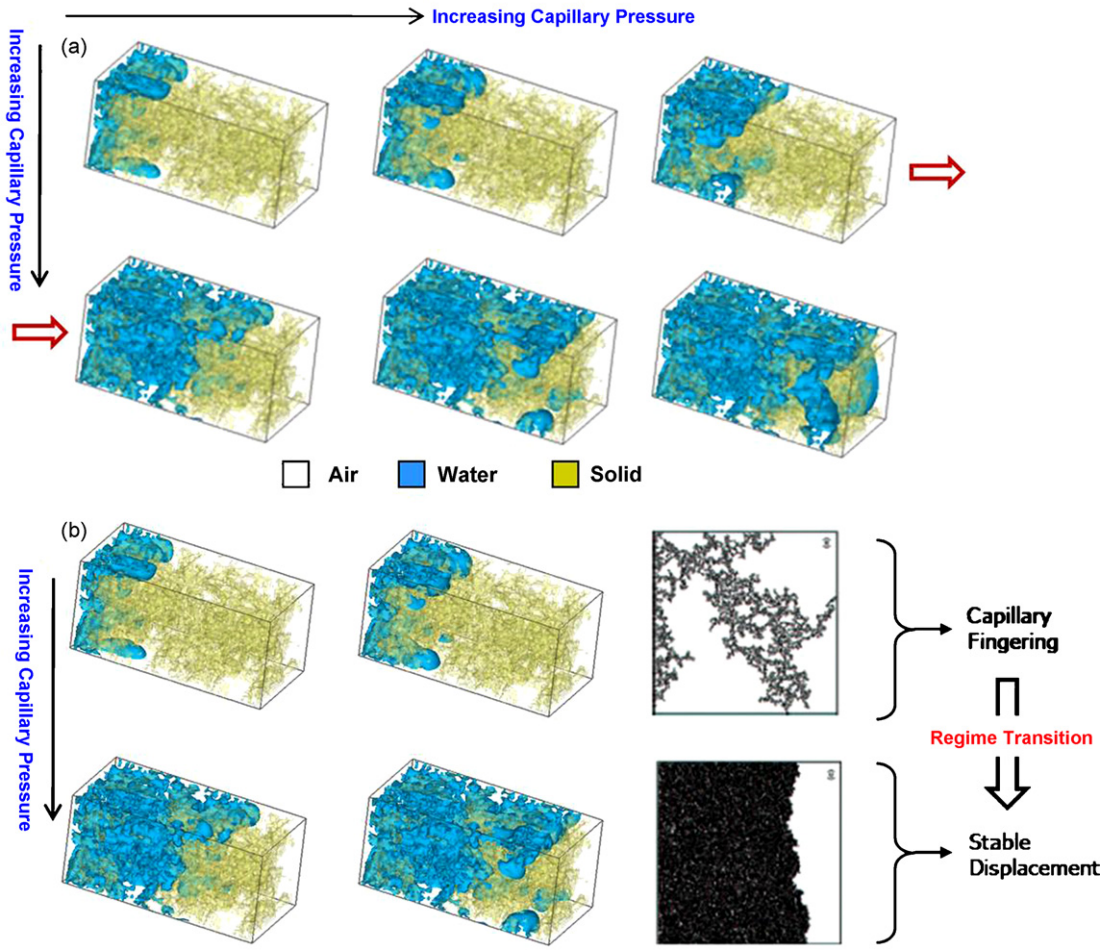

Fig. 11. Advancing liquid water front with increasing capillary pressure through the initially air-saturated reconstructed CL microstructure from the primary drainage simulation.

CL structure with $100 \times 50 \times 50$ lattice nodes and a GDL structure with $100 \times 100 \times 100$ lattice nodes. A typical simulation using ten computer nodes on a typical Linux PC cluster takes approximately 100–120 h to reach steady state for a particular saturation level.

4. Results and discussion

Fig. 11 displays the steady state invading liquid water fronts corresponding to increasing capillary pressures from the *primary drainage simulation* in the reconstructed CL microstructure characterized by slightly hydrophobic wetting characteristics with a static contact angle of 100°. At lower capillary pressures, the liquid water saturation front exhibits finger like pattern, similar to the displacement pattern observed typically in the capillary fingering regime. The displacing liquid water phase penetrates into the body of the resident wetting phase (i.e., air) in the shape of fingers owing to the surface tension driven capillary force. However, at high saturation levels, the invading non-wetting phase tends to exhibit a somewhat flat advancing front. This observation, as highlighted in Fig. 11(b), indicates that with increasing capillary pressure, even at very low Capillary number (Ca), several penetrating saturation fronts tend to merge and form a stable front. The invasion pattern transitions from the capillary fingering regime to the stable displacement regime and potentially lies in the transition zone in between. Further investigations with varying CL microstructures and wetting characteristics are currently underway to understand the two-phase regime transition dynamics in the PEFC electrode characterized by capillarity dominated flow behavior. In an operating fuel cell, the resulting liquid water displacement pattern pertaining to the underlying pore-morphology and wetting characteristics would play a vital role in the transport of the liquid water and hence the overall flooding behavior.

Fig. 12 shows the liquid water distribution as well as the invasion pattern from the *primary drainage simulation* with increasing capillary pressure in the initially air-saturated reconstructed carbon paper GDL characterized by hydrophobic wetting characteristics with a static contact angle of 140°. It is to be noted that the reconstructed GDL structure used in the two-phase simulation consists of $100 \times 100 \times 100$ lattice points as opposed to the high resolution structure with $512 \times 512 \times 512$ lattice points shown in Fig. 2 in order to manage the computational overhead to a reasonable level. Physically, this scenario corresponds to the transport of liquid water generated from the electrochemical reaction in a hydrophobic CL into the otherwise air-occupied GDL in an operating fuel cell. At the initially very low capillary pressure, the invading front overcomes the barrier pressure only at some preferential locations depending upon the pore size along with the emergence of droplets owing to strong hydrophobicity. As the capillary pressure increases, several liquid water fronts start to penetrate into the air occupied domain. Further increase in capillary pressure exhibits growth of droplets at two invasion fronts, followed by the coalescence of the drops and collapsing into a single front. This newly formed front then invades into the less tortuous in-plane direction. Additionally, emergence of tiny droplets and subsequent growth can be observed in the constricted pores in the vicinity of the inlet region primarily due to strong wall adhesion forces from interac-

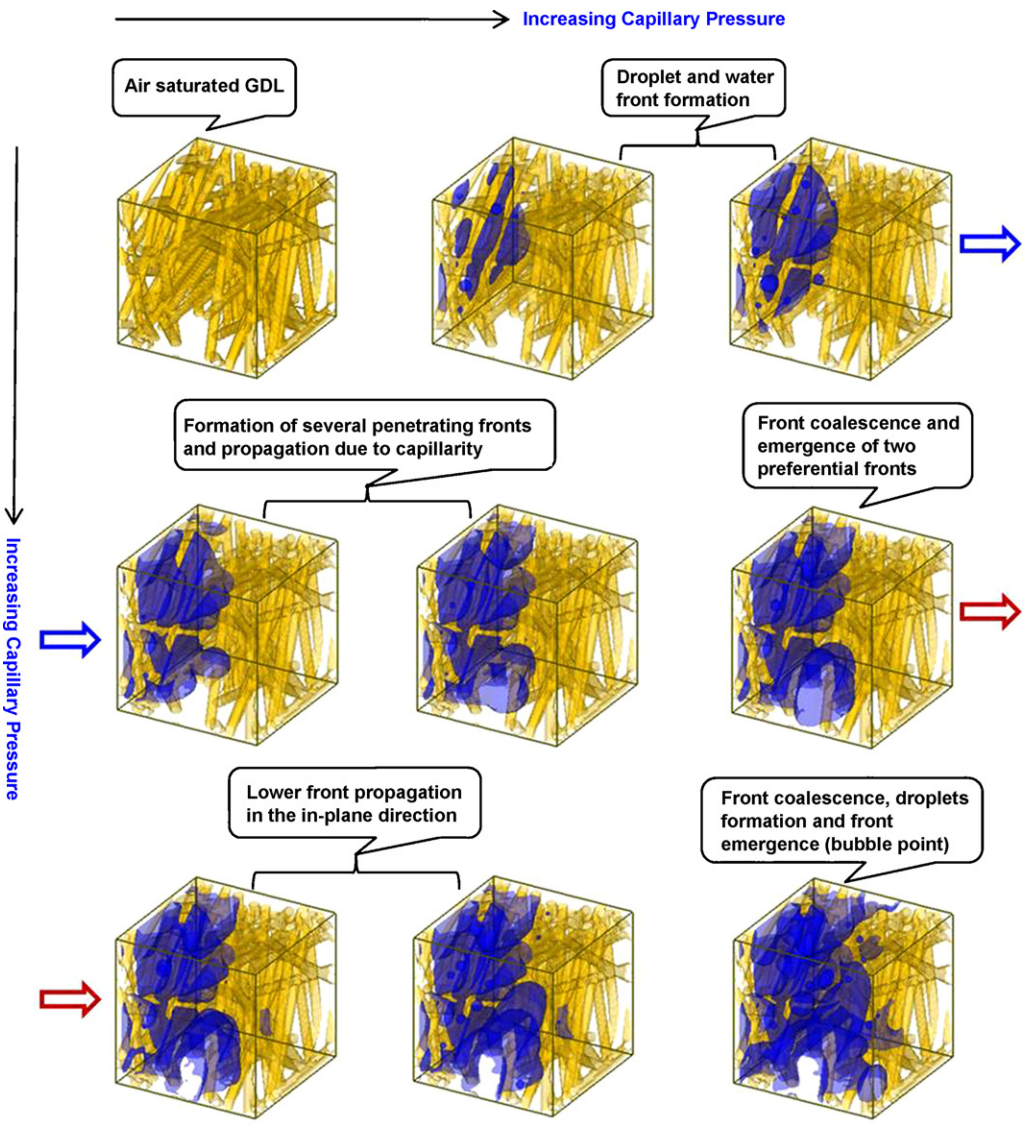

Fig. 12. Advancing liquid water front with increasing capillary pressure through the initially air-saturated reconstructed GDL microstructure from the primary drainage simulation.

tions with highly hydrophobic fibers with the increasing capillary pressure. One of the several invading fronts finally reaches the air reservoir, physically the GDL/channel interface, at a preferential location corresponding to the capillary pressure and is also referred to as the bubble point. Additionally, the 2D liquid water saturation maps at different cross-sections along the GDL through-plane direction corresponding to a representative liquid water saturation level are shown in Fig. 13 which demonstrates the porous pathways actually available for oxygen transport from the channel to the CL reaction sites. It is worth mentioning that the LB simulation is indeed able to capture the intricate liquid water dynamics including droplet interactions, flooding front formation and propagation through the hydrophobic fibrous GDL structure. Furthermore, it is important to note that the liquid water transport and flooding dynamics through a woven carbon cloth GDL would lead to very different scenario owing to liquid water motion along individual fibers as well as between fiber bundles as opposed to that in the non-woven carbon cloth GDL. Detailed investigations are currently underway to understand the influence of different pore morphology and wetting characteristics of GDL structures on the resulting flooding dynamics and will be reported in a future communication. It is important to note that the mesoscopic LB simulations provide fundamental insight into the pore-scale liquid water transport through different GDL structures and would likely enable novel GDL design with better water removal and flooding mitigation. Further primary drainage simulations using the two-phase LB model are currently underway to understand the capillary behavior and predict the capillary–pressure relations as functions of liquid water saturation for disparate microstructure–wettability characteristics of the CL and the GDL. Especially, the predicted bubble point pressures and the capillary pressure–saturation relations for different GDL structures from these simulations will be compared with the recent experimental measurements [57–60] reported in the literature and will be communicated in a future publication. It is also important to note that there is hardly any such experimental measurement yet available in the literature for the thin PEFC electrode due to the inherent complexity of a viable experimental method of two-phase displacement in the CL.

Fig. 14 exhibits the 3D liquid water distributions corresponding to several low saturation levels (below 15%) for the CL from the *steady state flow simulation* at equilibrium. It can be observed that below 10% saturation level there is hardly any connected pathway for the liquid water phase to transport through the CL structure and hence the relative mobility of the liquid water phase with

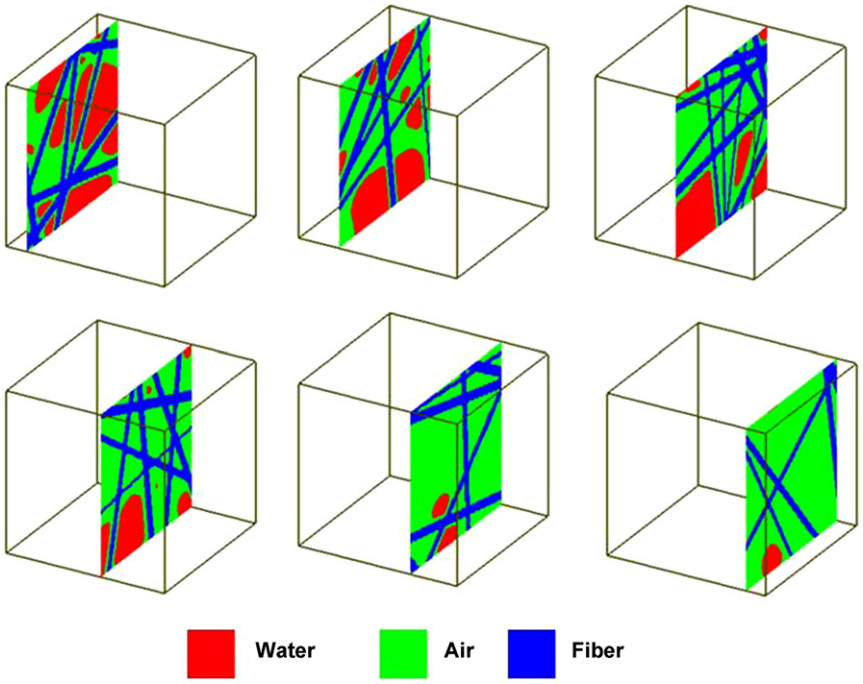

Fig. 13. 2D phase distribution maps on several cross-sections along the GDL through-plane direction from the primary drainage simulation.

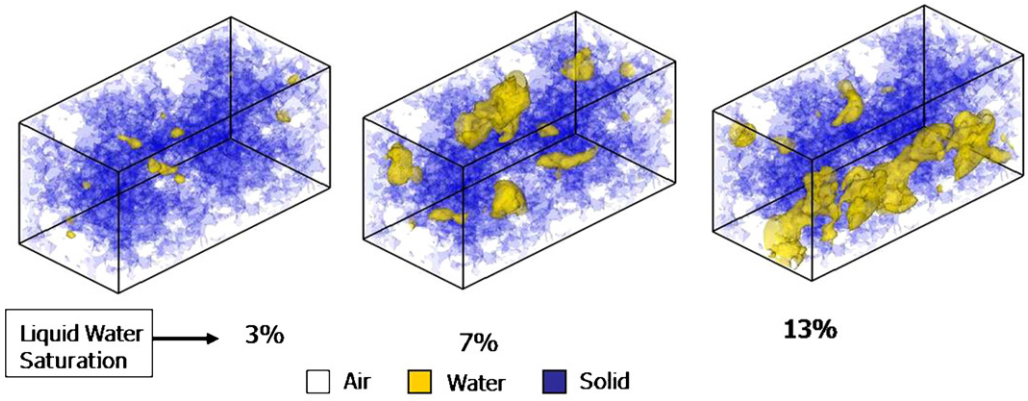

Fig. 14. 3D liquid water distributions in the reconstructed CL microstructure from the steady state flow simulation at equilibrium.

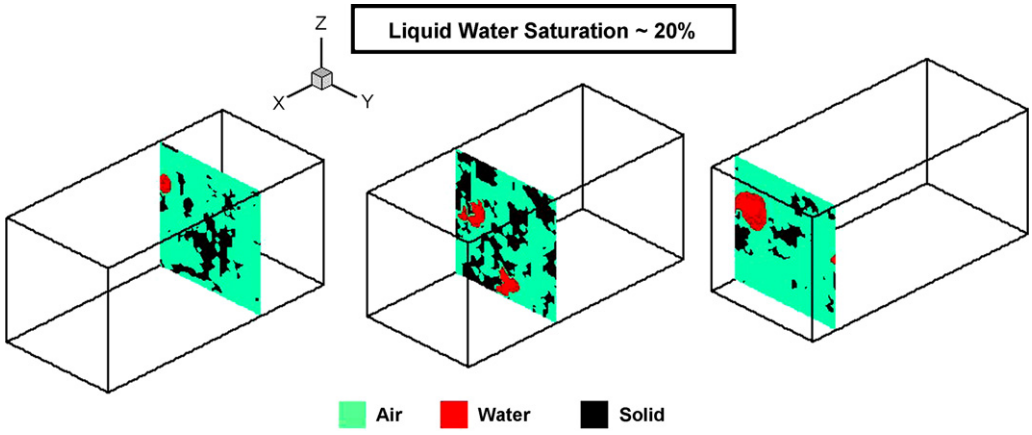

Fig. 15. 2D phase distribution maps in the reconstructed CL microstructure from the steady state flow simulation at equilibrium.

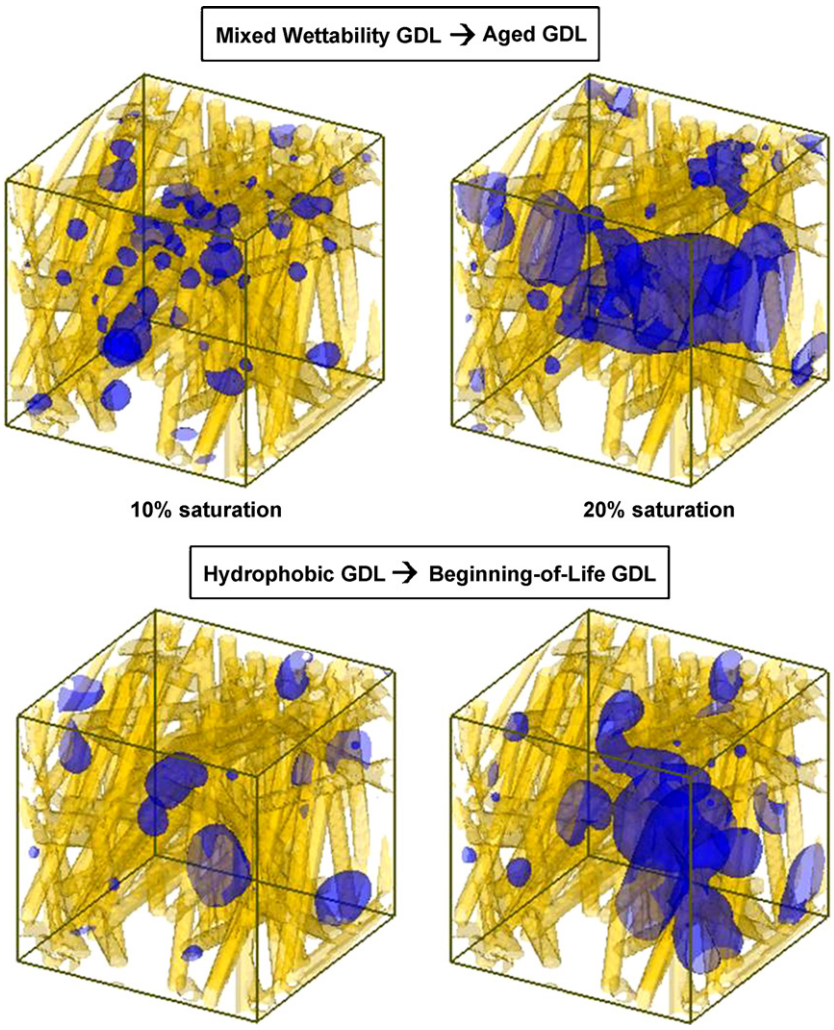

Fig. 16. 3D liquid water distributions in a hydrophobic and a mixed wettability GDL from the two-phase LB simulations.

respect to the incumbent air phase is negligible. As the saturation level increases, the initially random liquid water phase redistributes owing to the action of capillarity and finds a connected pathway for transport through the CL structure. The major significance of this numerical experiment is that based on the pore structure, wetting characteristics and two-phase dynamics at the phase interface, the relative permeability, which is the most important two-phase correlation, can be evaluated as a function of liquid water saturation [20]. Fig. 15 shows the 2D liquid water saturation maps corresponding to a representative saturation level of 20% on several cross-sections along the thickness of the reconstructed CL. The implication of the 2D saturation maps is that the reduction in electrochemically active area (ECA) owing to liquid water coverage in the CL can be estimated and the detrimental consequence of liquid water on the CL electrochemical performance can be quantified [61]. Furthermore, it is imperative to emphasize that this pore-scale two-phase model delineates the impact of the underlying structure and wetting characteristics of the CL on liquid water distribution and dynamics which would subsequently influence the relative phase mobility and transport.

Fig. 16 shows the equilibrium liquid water distribution after the randomly dispersed initial liquid water redistributes by the action of capillary force for a purely hydrophobic GDL with contact angle of around 140° and also for a mixed wettability GDL with hydrophilic and hydrophobic contact angles of 80° and 140°, respectively. In the mixed wettability GDL, a hydrophilic pore fraction of 50% is considered and the hydrophilic pores are assumed to be randomly distributed in the GDL structure. It can be observed that at similar saturation level, the liquid water distribution is quite different for the two GDLs, underscoring the influence of the wetting characteristics and interfacial dynamics on liquid water transport. In the mixed wettability GDL, due to the hydrophilic pores, liquid water exhibits a somewhat stable front preferentially oriented along the through-plane direction. On the other hand, in a purely hydrophobic GDL, liquid water tends to distribute preferentially in the less tortuous in-plane direction and exhibits a narrow flooding front, which would facilitate effective oxygen transport along the through-plane direction from the gas channels to the CL active sites. The far reaching implication of this study is to understand the liquid water behavior and flooding dynamics in a beginning-of-life GDL which is predominantly hydrophobic as opposed to that in an ageing GDL after prolonged fuel cell operation leading to partially hydrophilic fibers [62,63] and mixed wetting characteristics thereby causing enhanced flooding and severe performance degradation. Further investigations are presently underway and the predictions from such studies will be presented in a future communication related to GDL durability influence on two-phase flooding phenomena. Additionally, Fig. 17 exhibits the 2D phase distributions on several cross-sections for a representative saturation level around 20%. The liquid water distributions from such study could be further used to quantify the averaged saturation-dependent effective transport properties (e.g. effective species diffusivity). Finally,

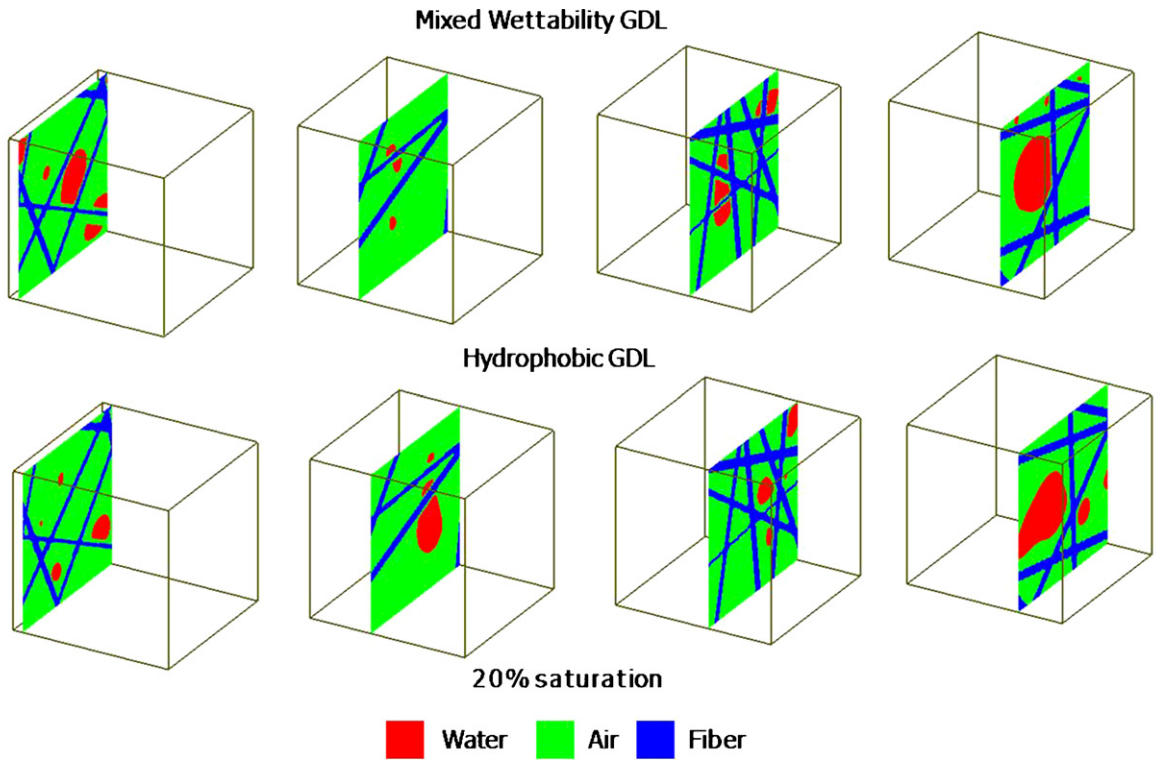

Fig. 17. 2D phase distribution maps on several cross-sections for a hydrophobic and a mixed wettability GDL from the two-phase LB simulations.

it is worth pointing out that the mesoscopic two-phase model not only captures the pore occupancy by liquid water due to pore size distribution but also phase redistribution owing to the underlying interfacial dynamics and wetting characteristics.

5. Conclusions

The catalyst layer and the gas diffusion layer play a crucial role in the overall PEFC performance due to the transport limitation in the presence of liquid water and flooding phenomena. The macroscopic two-phase fuel cell models cannot address the effects of the complex pore morphology and wetting characteristics on the liquid water transport. In this work, the development of a mesoscopic, two-phase lattice Boltzmann model coupled with stochastic microstructure reconstruction models is presented in order to reveal the structure–wettability influence on the underlying liquid water transport and flooding dynamics in the PEFC CL and GDL. The liquid water flooding front in the CL apparently tends to exhibit a transition from capillary fingering to somewhat stable displacement pattern even in a strictly capillary dominated flow regime and with benign wetting characteristics. The liquid water transport in the fibrous GDL characterized by highly hydrophobic fibers shows intricate interfacial dynamics including droplet interactions, flooding front formation and propagation. The influence of partially wetting pore structure on the flooding behavior is also elucidated for a mixed wettability GDL observed in an aged GDL. Finally, the overriding implications of the mesoscopic modeling formalism coupled with realistic microstructure reconstruction techniques lie in quantifying the structure–wettability–performance interlinks in the CL and GDL and fostering novel water management strategies for PEFCs.

Acknowledgements

PPM would like to thank V.P. Schulz, A. Wiegmann and J. Becker from Fraunhofer ITWM, Germany, for collaboration with GDL microstructure generation. Financial support from NSF through grant no. 0609727 and ECEC industrial sponsors is gratefully acknowledged.

Appendix A. Nomenclature

Bo	Bond number
Ca	Capillary number
f_i	particle distribution function in the ith direction
$G(\mathbf{x},\mathbf{x}')$	Green's function related to interparticle interaction
M	viscosity ratio
NWP	non-wetting phase
Re	Reynolds number
We	Weber number
WP	wetting phase

Greek symbols

ρ	phase density
μ	dynamic viscosity of phases
τ	relaxation time

Subscripts and superscripts

1	wetting phase
2	non-wetting phase

References

[1] C.Y. Wang, in: W. Vielstich, A. Lamm, H.A. Gasteiger (Eds.), Handbook of Fuel Cells—Fundamentals, Technology and Applications, vol. 3, John Wiley & Sons, Chichester, 2003, p. 337 (Chapter 29).
[2] C.Y. Wang, Chem. Rev. 104 (2004) 4727.
[3] Z.H. Wang, C.Y. Wang, K.S. Chen, J. Power Sources 94 (2001) 40.
[4] U. Pasaogullari, C.Y. Wang, J. Electrochem. Soc. 151 (2004) 399.
[5] U. Pasaogullari, C.Y. Wang, J. Electrochem. Soc. 152 (2005) A380.
[6] U. Pasaogullari, P.P. Mukherjee, C.Y. Wang, K.S. Chen, J. Electrochem. Soc. 154 (2007) B823.
[7] Y. Wang, C.Y. Wang, J. Electrochem. Soc. 153 (2006) A1193.

[8] Y. Wang, C.Y. Wang, J. Electrochem. Soc. 154 (2007) B636.
[9] A.Z. Weber, J. Newman, J. Electrochem. Soc. 152 (2005) A677.
[10] T. Berning, N. Djilali, J. Electrochem. Soc. 150 (2003) A1589.
[11] M. Noponen, E. Birgersson, J. Ihonen, M. Vynnycky, A. Lundblad, G. Lindbergh, Fuel Cells 4 (2004) 365.
[12] S. Dutta, S. Shimpalee, J.W. Van Zee, Int. J. Heat Mass Transfer 44 (2001) 2029.
[13] S. Mazumder, J.V. Cole, J. Electrochem. Soc. 150 (2003) A1510.
[14] J. Nam, M. Kaviany, Int. J. Heat Mass Transfer 46 (2003) 4595.
[15] W. He, J.S. Yi, T.V. Nguyen, AIChE J. 46 (2000) 2053.
[16] L. You, H. Liu, Int. J. Heat Mass Transfer 45 (2002) 2277.
[17] J.J. Baschuk, X. Li, J. Power Sources 86 (2000) 181.
[18] P.P. Mukherjee, C.Y. Wang, J. Electrochem. Soc. 153 (2006) A840.
[19] P.P. Mukherjee, C.Y. Wang, J. Electrochem. Soc. 154 (2007) B1121.
[20] P.P. Mukherjee, PhD Dissertation, The Pennsylvania State University, 2007.
[21] P.P. Mukherjee, G. Wang, C.Y. Wang, in: R.E. White, C.G. Vayenas, M.E. Gamboa-Aldeco (Eds.), Modern Aspects of Electrochemistry, vol. 40, Springer, New York, 2007, p. 285.
[22] P.M. Adler, Porous Media: Geometry and Transports, Butterworth-Heinemann, Stoneham, 1992.
[23] P.M. Adler, C.G. Jacquin, J.A. Quiblier, Int. J. Multiphase Flow 16 (1990) 691.
[24] D.P. Bentz, N.S. Martys, Transp. Porous Media 17 (1995) 221.
[25] H.A. Gasteiger, W. Gu, R. Makharia, M.F. Mathias, B. Sompalli, in: W. Lietsich, A. Lamm, H.A. Gasteiger (Eds.), Handbook of Fuel Cells—Fundamentals, Technology and Applications, vol. 3, John Wiley & Sons, Chicester, 2003, p. 517 (Chapter 46).
[26] S.S. Kocha, in: W. Lietsich, A. Lamm, H.A. Gasteiger (Eds.), Handbook of Fuel Cells—Fundamentals, Technology and Applications, vol. 3, John Wiley & Sons, Chicester, 2003, p. 517 (Chapter 43).
[27] M.F. Mathias, J. Roth, J. Fleming, W. Lehnert, in: W. Lietsich, A. Lamm, H.A. Gasteiger (Eds.), Handbook of Fuel Cells—Fundamentals, Technology and Applications, vol. 3, John Wiley & Sons, Chicester, 2003, p. 517 (Chapter 42).
[28] V.P. Schulz, J. Becker, A. Wiegmann, P.P. Mukherjee, C.Y. Wang, J. Electrochem. Soc. 154 (2007) B419.
[29] K. Schladitz, S. Peters, D. Reinel-Bitzer, A. Wiegmann, J. Ohser, Comput. Mater. Sci. 38 (2006) 56.
[30] S. Chen, G. Doolen, Annu. Rev. Fluid Mech. 30 (1998) 329.
[31] A.K. Gunstensen, D.H. Rothman, S. Zaleski, G. Zanetti, Phys. Rev. A 43 (1991) 4320.
[32] X. Shan, H. Chen, Phys. Rev. E 47 (1993) 1815.
[33] M.R. Swift, W.R. Osborn, J.M. Yeomans, Phys. Rev. Lett. 75 (1995) 830.
[34] X.Y. He, S.Y. Chen, R.Y. Zhang, J. Comput. Phys. 152 (1999) 642.
[35] P. Bhatnagar, E. Gross, M. Krook, Phys. Rev. 94 (1954) 511.
[36] H. Chen, S. Chen, W.H. Matthaeus, Phys. Rev. A 45 (1992) R5339.
[37] N. Martys, H. Chen, Phys. Rev. E 53 (1996) 743.
[38] X. Shan, G.D. Doolen, Phys. Rev. E 54 (1996) 3614.
[39] X. Shan, G.D. Doolen, J. Stat. Phys. 81 (1995) 379.
[40] S. Hou, X. Shan, Q. Zou, G. Doolen, W. Soll, J. Comput. Phys. 138 (1997) 695.
[41] C. Pan, M. Hilpert, C.T. Miller, Water Resour. Res. 40 (2004) 1.
[42] C. Pan, Ph.D. Dissertation, University of North Carolina, Chapel Hill, 2003.
[43] P. Lavallee, J.P. Boon, A. Noullez, Physica D 47 (1991) 233.
[44] F.A.L. Dullien, Porous Media: Fluid Transport and Pore Structure, Academic Press, San Diego, CA, 1992.
[45] Z.L. Yang, T.N. Dinh, R.R. Nourgaliev, B.R. Sehgal, Int. J. Heat Mass Transfer 44 (2001) 195.
[46] Q. Kang, D. Zhang, S. Chen, Phys. Fluids 14 (2002) 3203.
[47] Q. Kang, D. Zhang, S. Chen, J. Fluid Mech. 545 (2005) 41.
[48] R. Lenormand, E. Touboul, C. Zarcone, J. Fluid Mech. 189 (1988) 165.
[49] R.P. Ewing, B. Berkowitz, Adv. Water Res. 24 (2001) 309.
[50] X.G. Yang, F.Y. Zhang, A. Lubawy, C.Y. Wang, Electrochem. Solid-State Lett. 7 (2004) A408.
[51] J. Bear, Dynamics of Fluids in Porous Media, Dover, New York, 1972.
[52] D. Tiab, E. Donaldson, Petrophysics: Theory and Practice of Measuring Reservoir Rock and Transport Properties, Gulf Publishing Company, Houston, 1996.
[53] D.W. Grunau, Ph.D. Dissertation, Colorado State University, 1993.
[54] D.G. Avraam, A.C. Payatakes, Transp. Porous Media 20 (1995) 135.
[55] P.P. Mukherjee, C.Y. Wang, Proceedings of the ASME Fuel Cell 2008, 6th ASME International Fuel Cell Science, Engineering and Technology Conference, Denver, CO, USA, June 16–18, 2008.
[56] H. Li, C. Pan, C.T. Miller, Phys. Rev. E 72 (2005) 026705.
[57] J. Benziger, J. Nehlsen, D. Blackwell, T. Brennean, J. Itescu, J. Membr. Sci. 261 (2005) 98.
[58] J.T. Gostick, M.W. Fowler, M.A. Ioannidis, M.D. Pritzker, Y.M. Volfkovich, A. Sakars, J. Power Sources 156 (2006) 375.
[59] J.D. Fairweather, P. Cheung, J. St-Pierre, D.T. Schwartz, Electrochem. Commun. 9 (2007) 2340.
[60] K.G. Gallagher, R.M. Darling, T.W. Patterson, M.L. Perry, J. Electrochem. Soc. 155 (2008) B1225.
[61] P.P. Mukherjee, C.Y. Wang, ECS Trans. 3 (2006) 1085.
[62] P.K. Sinha, P.P. Mukherjee, C.Y. Wang, J. Mater. Chem. 17 (2007) 3089.
[63] D.L. Wood III, R.L. Borup, in: F.N. Buchi, M. Inaba, T.J. Schmidt (Eds.), Polymer Electrolyte Fuel Cell Durability, Springer, New York, 2009, p. 159.